

Research

Exploring torque characteristics of an integrated ultra-conducting magnetic coupling incorporating axial magnetic field through magnetic equivalent circuit modelling

Patrick Ombolo Djomo¹

Received: 8 January 2024 / Accepted: 18 June 2024

Published online: 05 July 2024

© The Author(s) 2024 [OPEN](#)

Abstract

Ultra-conductors are a recent class of materials that display superconducting attributes at room temperature and even at higher temperatures. In this paper, we introduce a novel hybrid ultra-conducting coupling (NHUC) where the secondary component includes copper and an ultra-conductor (considered as a room temperature superconductor in much research). We suggest a model based on magnetic equivalent circuit (MEC) to evaluate the distribution of magnetic fields and characteristics related to torque. The 3D model accounts for boundary impacts during mating, and formulation for magnetic flux and torque are derived using Kirchhoff's and Ampere's loop laws, respectively. A 3D finite element (FEM) model is constructed, and simulations are performed using iodine-doped double-walled carbon nanotube (IDWCT) as the ultra-conductor for a wider operating range. At a high slip speed of 1200 rpm, a maximum torque of 309 Nm and stable torque of 113 Nm are observed. Adjusting air gap thickness or permanent magnet dimensions results in torque variations. Additionally, due to carbon nanotube (CNT) characteristics, a reduction in losses from the Joule effect is noted. The maximum error between torque results from simulation and the suggested model is 7.68%, confirming accordance. Comparison alongside the slotted eddy current coupling (SEC) reveals that the torque of the NHUC exceeds that of the SEC, diminishing as the air gap widens.

Keywords Hybrid · Ultra-conducting magnetic coupling · Carbon nanotube composite (CNT) · Magnetic equivalent circuit (MEC) · Ultra-conductor · Torque

1 Introduction

Eddy current couplers are increasingly gaining interest as torque transfer devices due to their advantages over traditional connections [1], such as stability, high reliability, easy maintenance, noise reduction, and a good vibration isolation effect. However, the development of an accurate model is essential for studying the performance of a permanently magnetized eddy current magnetic coupler (PMEC). Previous research has proposed various analytical models for PMEC couplers by combining equivalent magnetic circuits with the laws of Faraday's and Ampère to handle complex geometries [2–11]. These models take into account the magnetomotive force and reaction field caused by eddy currents in the conductor, predicting torque characteristics and reaction flux [12]. Furthermore, segmentation methods have been employed to

Supplementary Information The online version contains supplementary material available at <https://doi.org/10.1007/s44291-024-00013-2>.

✉ Patrick Ombolo Djomo, yangchaojun@ujs.edu.cn | ¹School of Mechanical Engineering, Jiangsu University, Zhenjiang 212013, China.



divide the magnetic field of PMEC into distinct areas. This division facilitates the calculation of the magnetoresistance for each individual area [13]. A mixed two-dimensional analytical modeling approach was proposed to obtain expressions for eddy current, magnetic field, electromagnetic force, and torque in such devices [14]. Additionally, a 3D analytical model describing the magnetic field of an axial-flux PMEC was proposed [15] to predict eddy current loss under various loads. Furthermore, the introduction of new materials in eddy current couplings to improve their efficiency is becoming popular. One recent study proposed an eddy current coupling with the secondary [16] consisting of a split superconductor and copper [17], while the development of composite conductors incorporating carbon nanotube and copper has introduced a novel aspect in the design of electric machines, offering the potential to enhance machine performance [18]. The findings demonstrate that the enhanced conductivity of the winding broadens the effectiveness chart, expanding the range of high-efficiency operation to include both light load and high-speed conditions. In this study, the conductive disk of the NHUC is a composite structure comprising alternating layers of copper and ultra-conductor enclosed within a steel crankcase from the patent [19]. During motion, magnetic flux can traverse through the copper and to a lesser extent through the ultra-conductor owing to the extremely low permeability of ultra-conductors. However, the diamagnetic characteristics of the ultra-conductor, surrounded by a high magnetic flux, cause some magnetic flux lines to be repelled toward the copper, thereby amplifying the production of induced currents within copper. Eddy currents the distribution undergoes alteration due to the use of different materials, introducing complexity in calculating the reaction field. Considering the issues mentioned above, an MEC model has been developed to examine the torque properties of the NHCC. It has been confirmed that copper conductor serves as the primary heat source into magnetic coupling due to the circulation of eddy current and its electric conductivity is closely influenced by the heat [5]. However, the ultra-conductor plays a critical role in dissipating the heat generated by the copper. Ultra-conductor is specially engineered to possess a significantly higher heat dissipation coefficient compared to copper this means they are much more effective at transferring heat away from the source. The mechanism by which the overheating generated by the copper is mitigated is through conduction. Conduction refers to the transfer of heat energy through a material due to the movement of electrons or phonons (vibrational energy quanta). In this case, as the copper component heats up, the excess thermal energy is conducted through the adjacent ultra-conductor. The superior heat dissipation coefficient of the ultra-conductor facilitates rapid and efficient transfer of heat away from the copper. This is achieved because of the exceptionally strong heat conduction of the ultra-conductor. so by utilizing ultra-conductor with superior heat dissipation properties, permit to optimize the device thermal management. This ensures that the heat generated by the copper conductor is effectively evacuated, maintaining optimal operating conditions, and preventing potential damage. In this article, our primary focus lies on the electromagnetic aspect. However, it is important to note that our forthcoming publication will delve into the thermal analysis of our magnetic coupling as its central theme.

The key goals of this research are:

1. To examine the performance of the composite conductor under low speed in a magnetic coupling.
2. To investigate the consistency of the system during high-velocity and low-velocity situations.
3. To depict the trajectories of eddy currents and magnetic fields.
4. To establish the coupling's torque via the modulation of the air gap and the width of PMs.
5. To create a MEC model for the design, to measure torque's outcomes and contrast them with simulation-based results.

This research and the techniques employed demonstrate that the coupling is functional under standard pressure and temperature levels.

2 Background and history

Ultra-conductors, often referred to as room temperature superconductors, are gaining widespread attention for their potential applications in large-scale power systems utilized by both industrial end-users and electric utilities. Kumar [20] researcher have found that when ultra-conductor are used to replace copper and aluminum, losses are decreased by 45% and 67%, respectively [21–23]. Moreover, a recent study proposed a permanent-magnet machine with carbon-based conductors [24], which demonstrated that ultra-conductor possess high electrical and thermal conductivity and low mass density. This breakthrough technology could be instrumental in achieving a more power-dense eddy current coupling. In refs. [25, 26] proposed integrating copper (Cu) with carbon nanotubes (CNTs) to form a freestanding ultra-conductor. Also [27], an ultra-conductor based on magnesium, with a purity of 99.999% and electrical conductivity

on the order of 10^{16} S/m when subjected to a temperature of 360 K. Rallabandi et al. [28] studied Axial flux machines are gaining popularity because of their dense design. The ratio of torque to weight may be significantly improved by employing windings made of carbon nanotubes. In the same direction [18] conducted a study to assess the extent which a carbon nanotube-copper composite enhances power per unit volume and the overall performance of electric motors.

3 Recent findings

3.1 Suggested design

According to the patent document (CNPatent CN114337188B) [19] the suggested Design, as depicted in Fig. 1, incorporates a primary composed of a steel disc housing permanent magnet (PMs). The S-pole is negative, while the N-pole is positive. The permanent magnets are spaced apart via thin metal layers. As shown in Fig. 1c, the secondary is made of copper and ultra-conductor arranged in a steel disc. In this study, the ultra-conductor used is the iodine-doped carbon nanotube (IDWCT), which has a conductivity higher than copper. This ultra-conductor can be prepared in four steps: Synthesize nanotubes, refinement, immersion in vitriol, and contraction [29, 30].

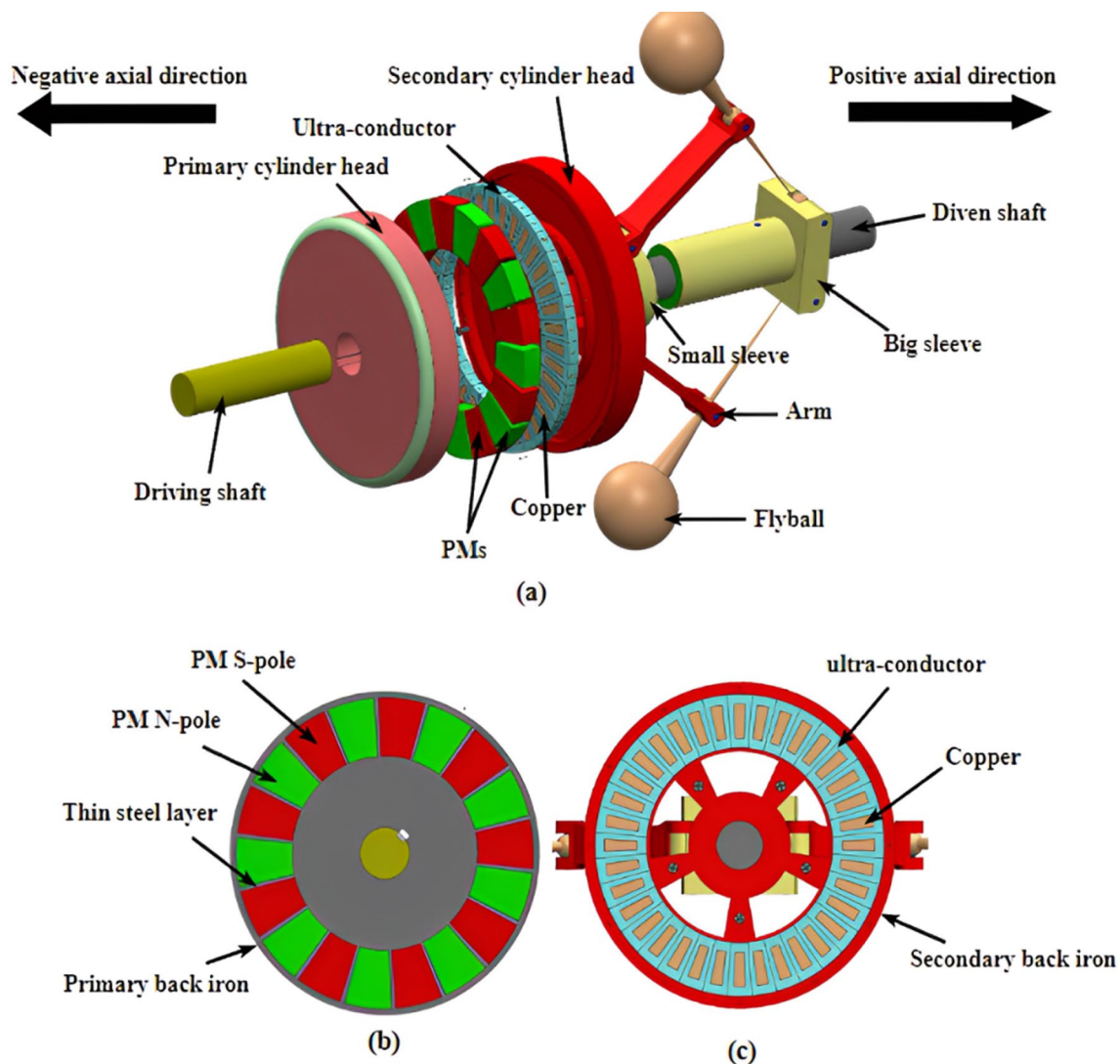


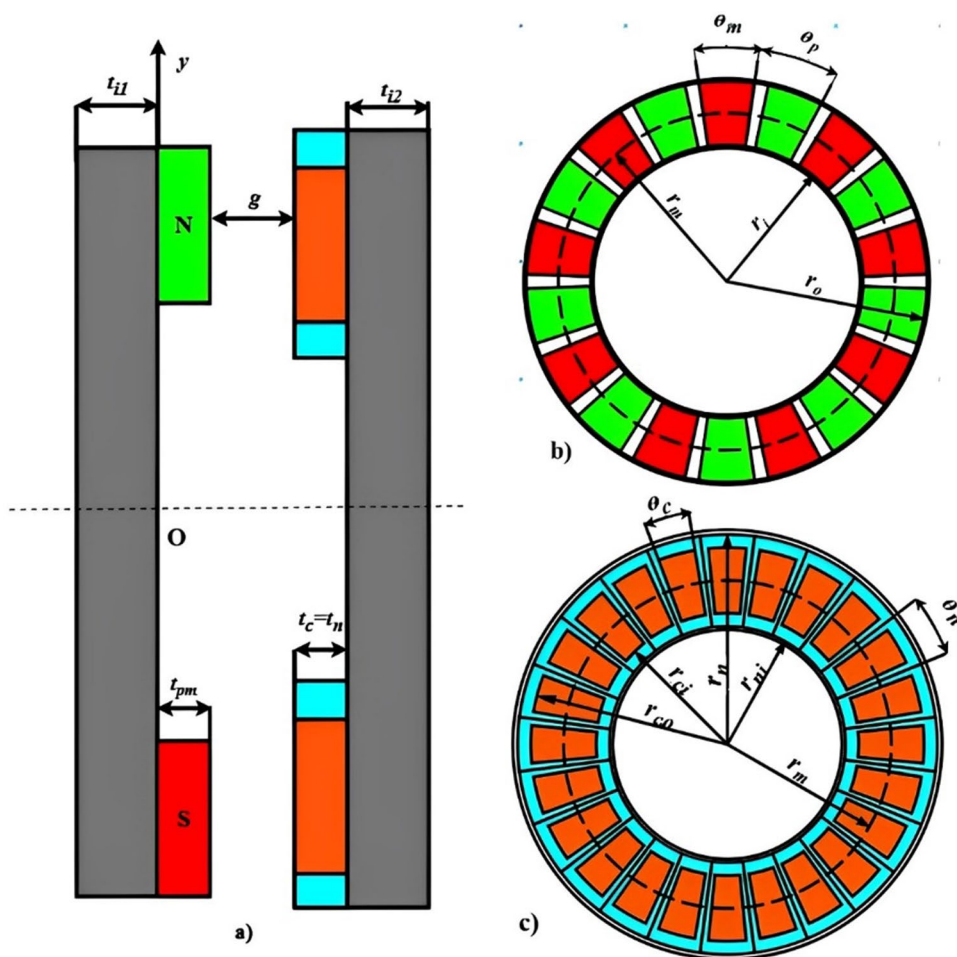
Fig. 1 Illustration of the suggested design (a), leading disc (b), led disc (c)

In this study, our focus is solely on the magnetic characteristics, and we do not take temperature effects into account. The ultra-conductor, with a permeability relatively close to 0, allows most flux lines to pass through copper, which has a higher permeability. Additionally, ultra-conductors exhibit diamagnetic properties in the presence of high magnetic flux, repelling a portion of the flux lines towards copper, thereby increasing eddy current generation. The variation of the magnetic flux within the space induces current inside both copper and ultra-conductor, leading to three different eddy current paths, as illustrated in Fig. 8. The first path involves eddy current circulating only in copper, the second path only in the ultra-conductor, and the third path passing through both conductors. However, for the purpose of this study, we consider only the paths of eddy current passing through both conductors. We leverage this feature to compensate for the losses generated by copper and maintain a consistent torque. The use of the ultra-conductor is implemented to enhance the magnetic flux in the air space, causing a large and constant density of flux and a substantial decrease in losses due to Joule effects.

3.2 Theory

Figure 2 depicts the profile and NHUC's geometric features. The surface-installed PMs, magnetized longitudinally, are positioned interchangeably on the leading disc back yoke. The copper and ultra-conductor are integrated into the disc back yoke. The ultra-conductor serves to confine the magnetic flux that cannot pass through it due to its low permeability, preventing losses from the Joule effect. The magnetic field is captured through induced currents resulting from the varying magnetic flux implemented to the ultra-conductor. Additionally, the ultra-conductor is utilized for screening purposes, relying on the induction of current in the superconducting material for magnetic field screening. The emergence of these currents acts in opposition to the magnetic flux produced by the PMs, resulting in a semi-diamagnetic behavior of the ultra-conductor. This property of the ultra-conductor is utilized here to direct a substantial portion of

Fig. 2 NHUC's structure (a) leading disk 2D perspective (b) led disk 2D perspective (c)



the magnetic flux attempting to traverse it in the direction of the air gap or copper. Results in a significant density of flux and a notable decrease in deficits due to Joule effect. The details of the investigated design are summarized in Table 1.

1) Basic assumptions and 2D model

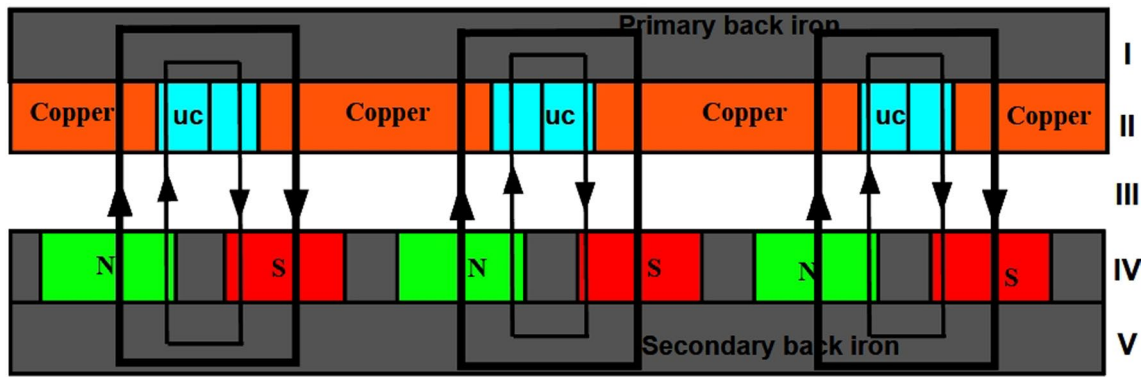
To simplify the estimation of induced currents and magnetic field produced via the led disc throughout its motion, the coupling is elongated beside the surrounding orientation on median length $r_m = (r_1 + r_2)/2$. This simplification transforms the three-dimensional model into a two-dimensional model, and the subsequent plausible conjectures are adopted.

- The principal magnetic flux crosses the PMs, space, and led disc vertically. The Permanent magnets are uniformly magnetized in the longitudinal orientation.
- The relative permeabilities of Permanent magnets, air, copper, and ultra-conductor are $\mu_a = 4\pi \times 10^{-7}$, $\mu_{pm} = 1.0997785406$, and $\mu_c = 0.99991$, $\mu_n = 4\pi \times 10^{-7}$ respectively.
- The leading disc and led disc back yoke thicknesses are sufficient to prevent magnetic saturated state. Therefore, their permeabilities were assumed to be limitless, and their resistances were neglected. The difference between our proposed model and previous magnetic couplings is that the secondary on the last magnetic coupler is made of conductor only. Meanwhile, the NHUC is made of ultra-conductor and conductor. The magnetic field distribution within NHUC undergoes continuous changes during its motion. Consequently, a two-dimensional model is formulated build on the earlier conjectures, as illustrated by Fig. 2. Figure 3a depicts the entire coupling magnetic network. It is noteworthy that the magnetic flux is particularly pronounced at the touch area neighboring PMs. Additionally, it is observed that the magnetic field lines are more substantial where they intersect with the copper compared to the ultra-conductor. This discrepancy arises from the redirection (outward repulsion) of a portion of the magnetic field attempting to traverse the ultra-conductor towards the copper. In Fig. 3b, both flux leakages (illustrated in dotted strokes) and paths of magnetic flux (depicted in continuous strokes) are presented within the leading disk, the led disc disk, and the ultra-conductor disk. The leakage flux (dotted strokes) comprises three components: firstly, the leakage occurring amidst contiguous PMs; secondly, the leakage amidst PMs and leading disc back iron; finally, the leakage flux amidst contiguous permanent magnets and iron located amidst them.
- Development of the magnetic equivalent circuit model

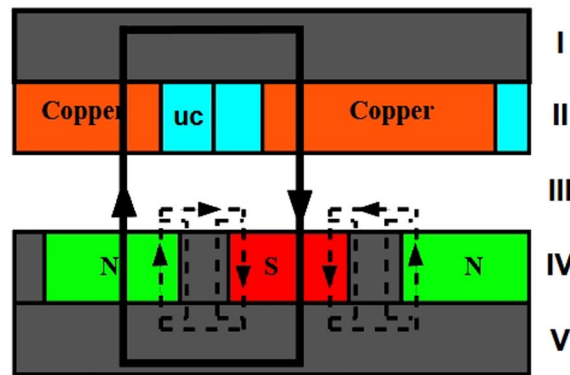
To formulate the magnetic equivalent circuit, we examine the magnetic flux routes, considering only half of the permanent magnets pair of poles. Given the uniformity of the magnetic flux paths in the NHUC, we construct an initial MEC model, illustrated in Fig. 4. It's important to note that every segment permeability is null in instances where a segment is absent at that precise location. The ultra-conductor does not possess zero reluctance, and the reaction

Table 1 Parameters of the proposed NHUC

Symbol	Description	Value	Symbol	Description	Value
t_c	Copper thickness	10 mm	σ_2	Conductivity of the ultra-conductor	$> \sigma_1$
t_n	CNT thickness	10 mm	σ_1	Conductivity of the copper	58MS
t_{pm}	PM thickness	10 mm	σ_i	Conductivity of the back iron	2MS
t_{j1}	Primary yoke length	10 mm	θ_c	Angle of the copper core	22°
t_{j2}	Secondary yoke length	10 mm	θ_n	Angle of the ultra-conductor	30°
r_i	PM inner radius	85 mm		ultra-conductor Density	$3800 \rho \text{ kg/m}^3$
r_o	PM outer radius	125 mm		Material of back iron	Steel 1010
p	Number of PM pole pair	9		Material of conductor	Copper, IDWCT
θ_m	Angle of pole pairs	20°	r_{no}	ultra-conductor outer radius	128 mm
r_m	Mean radius of PMs	95 mm	r_{ni}	ultra-conductor inner radius	72 mm
H_c	Coercivity of the PMs	-868 KA/m	r_j	Copper outer radius	120 mm
Δh	Overhang length	5 mm	r_o	Copper inner radius	80 mm
g	Air gap length	variable	α_c	Copper density	$8800 \rho \text{ kg/m}^3$
			α_n	Copper heat transfer coefficient	$400 \text{ W/(m}^2 \text{ K)}$
				UC heat transfer coefficient	$5000 \text{ W/m}^2 \text{ K}$



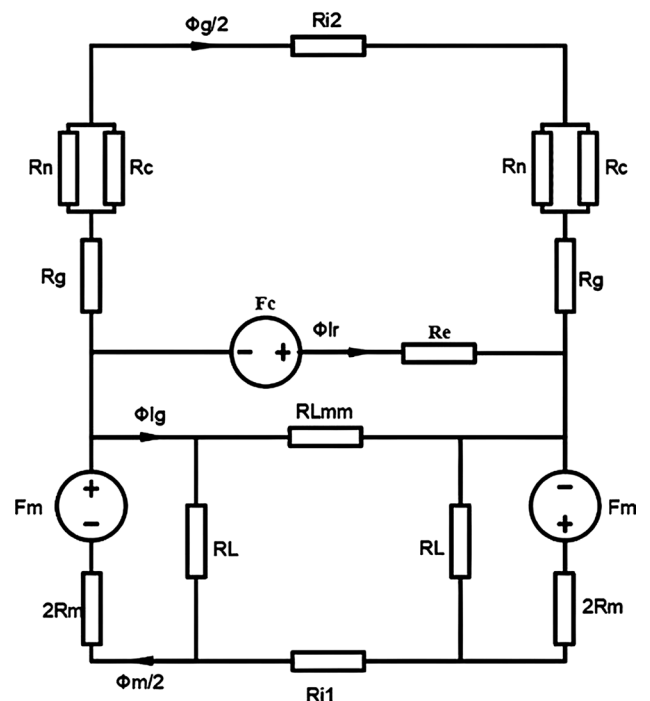
a)



b)

Fig. 3 NHUC's 2-D analytical design **a** entire, **b** division. (I: led disk back yoke; II: copper and ultra-conductor layer; III: air gap; IV: PMs setup; V: leading disk back yoke)

Fig. 4 Initial MEC model



flux resulting from eddy currents in both the conductor and the ultra-conductor cannot be disregarded. It's vital to highlight that Fig. 4 presents an intricate model and poses challenges for analysis. Consequently, a streamlined model has been devised, depicted in Fig. 5, to facilitate calculations.

An equivalent 2D configuration is employed through the linear expansion of the arrangement alongside the median of the active part r_m . The pole spacing and the various average arc lengths could be articulated in the following manner:

$$\begin{cases} \tau_m = r_m \theta_m \\ \tau_c = r_{mc} \theta_c, \tau_n = r_{mn} \theta_n \\ \tau_p = 2\pi r_m / p \end{cases} \quad (1)$$

Here, τ_m , τ_c , and τ_n represent the average arc lengths of PM, copper, and carbon nanotube, respectively. Additionally, τ_p stands for the mean pole pitch of the PMs, r_{mc} denotes the mean radius of copper, and r_{mn} indicates the mean radius of ultra-conductor.

The magnetomotive force and reluctance of a permanent magnet can be described by the following equation:

$$F_m = H_c t_{pm} \quad (2)$$

where H_c is the coercivity of the PM

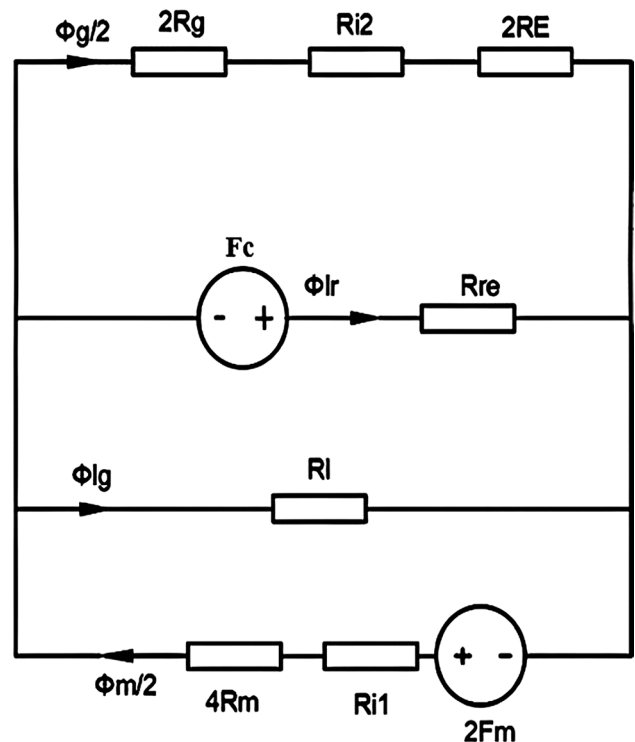
$$R_m = \frac{t_{pm}}{\mu_0 \mu_{rm} \tau_m (r_o - r_i)} \quad (3)$$

Reluctance of the copper can be given as mentioned.

$$R_c = \frac{t_c}{\mu_0 \tau_c (r_o - r_i)} \quad (4)$$

Reluctance of the ultra-conductor is given by the expression.

Fig. 5 Simplified MEC Model



$$R_n = \frac{t_n}{\mu_0 \tau_n (r_o - r_i)} \quad (5)$$

The reluctance of the leading disk back yoke and the led disk back yoke can be provided by:

$$R_{i1} = \frac{t_{yp}}{\mu_0 \tau_p (r_o - r_i)} \quad (6)$$

$$R_{i2} = \frac{t_{ys}}{\mu_0 \tau_p (r_o - r_i)} \quad (7)$$

The reluctance of the air gap is expressed in the ensuing manner:

$$R_g = \frac{t_g}{\mu_0 \tau_m (r_o - r_i)} \quad (8)$$

The pathways of flux corresponding to the reluctances of the leakage flux R_L and R_{Lmm} are pictured in Fig. 3. It is evident that the leakage flux's integration trajectory between adjacent Permanent magnets consists of linear section within the permanent magnets. the leakage flux's integration trajectory between adjacent permanent magnets and leading disk back yoke comprises a linear section inside the Permanent Magnets and semi-arc of the air gap.

The equations of R_{Lmm} and R_L can be expressed as:

$$R_{Lmm} = \frac{\pi}{\mu_0 (r_o - r_i) \left(\ln \left| \tau_p - \tau_m + 2t_{pm} + \pi r_{Lmm} \right| - \ln \left| 2t_{pm} + \tau_p - \tau_m \right| \right)} \quad (9)$$

$$R_L = \frac{(\pi + 2)t_{pm}}{2r_L \mu_0 (r_o - r_i)} \quad (10)$$

The magnitudes of the integration trajectories r_{Lmm} and r_L are expressed in accordance with the theory of minimum reluctance formulated as:

$$r_{Lmm} = \min \{ g + t_c / 2 \} \quad (11)$$

$$r_L = \min \{ t_{pm}, (\tau_p - \tau_m) / 2 \} \quad (12)$$

The reluctances R_1 and R_{lg} in Fig. 4. is given by:

$$R_1 = R_c // R_n \quad (13)$$

$$R_1 = \frac{R_c \times R_n}{R_n + R_c} \quad (14)$$

$$R_{lg} = 2R_L // R_{Lmm} \quad (15)$$

$$R_{lg} = \frac{R_L \times R_{Lmm}}{R_L + 2R_{Lmm}} \quad (16)$$

3) Determination of induced current reaction effect

The led disk region comprises both copper and ultra-conductor, which exhibit distinct electrical conductivities. To accurately represent the behavior of this heterogeneous material, the concept of effective conductivity is essential.

It considers the combined influence of both materials and provides a more accurate representation of their collective behavior. Copper and ultra-conductor have differing electrical conductivities, and their interaction within the conductor region affects the flow of eddy currents. By using effective conductivity, we capture the overall electrical behavior of the composite conductor, accounting for the interactions between the two materials. Calculate the effective electrical conductivity of the conductor region when both materials are present.

$$\sigma_{eff} = \frac{\sigma_1 \times \sigma_2}{\sigma_1 + \sigma_2} \quad (17)$$

where σ_1 and σ_2 are the electric conductivities of copper and conductor respectively. The mean magnetic flux density of the region travelling across the copper can be expressed as follows:

The mean magnetic flux density of the region crossing the conductor is formulated as:

$$B_m = \frac{\phi_g}{\tau_m(r_o - r_i)} \quad (18)$$

The formulation for the conductor's mean induced current density in the radial direction is represented as follows:

$$J_m = \frac{\sigma_{eff} \pi n_s r_m B_m}{30} \quad (19)$$

with n_s the slip speed amidst the permanent magnets and the led disk.

Hence, the representation of the magnetomotive force generated by induced currents in the led disk is as follows:

$$F_M = \int_{SJ} J \times ds = J_m(t_c \tau_m/2) = \sigma_{eff} \pi n_s r_m \tau_m / 60(r_o - r_i) \quad (20)$$

As stated, Appendix, at the midpoint x of the conductor thickness, the magnetic field density produced by the induced currents can be formulated as:

$$B_{re} = \begin{cases} \frac{\mu_0 J_m t_c}{2\pi} \ln \frac{\tau_p - x}{\tau_p - \tau_m/2 - x}, & 0 \leq x \leq \tau_m/2 \\ \frac{\mu_0 J_m t_c}{2\pi} \ln \frac{x(\tau_p - x)}{(x - \tau_m/2)(\tau_p - \tau_m/2 - x)}, & \tau_m/2 < x < (\tau_p - \tau_m/2) \\ \frac{\mu_0 J_m t_c}{2\pi} \ln \frac{x}{x - \tau_m/2}, & (\tau_p - \tau_m/2) \leq x \leq \tau_p \end{cases} \quad (21)$$

Therefore, the reaction flux is expressed as.

$$\phi_{re} = \int_0^{\tau_p} B_{re}(r_o - r_i) dx = \alpha \phi_g \quad (22)$$

With,

$$\alpha = \frac{\mu_0 \sigma_{eff} n_s r_m t_c}{60 \tau_m} \left[-2(\tau_p - \tau_m/2) \ln \left(\frac{(\tau_p - \tau_m/2)}{r_o - r_i} \right) + 2\tau_p \ln \left(\frac{\tau_p}{r_o - r_i} \right) - \tau_m \ln \left(\frac{\tau_m}{2(r_o - r_i)} \right) \right] \quad (23)$$

4) Magnetic fluxes equations

Utilizing the magnetic equivalent circuit model pictured by Fig. 5, a magnetic fluxes matrix is obtained from Kirchhoff's theorem. This matrix is articulated as mentioned:

$$\begin{pmatrix} \frac{R_{11}}{2} + 2R_m & R_{lg} & 0 \\ \frac{1}{2} & -1 & -\frac{1}{2} \\ 0 & R_{lg} & -(R_g + R_E + \frac{R_{12}}{2}) \end{pmatrix} \times \begin{pmatrix} \phi_m \\ \phi_{lg} \\ \phi_g \end{pmatrix} = \begin{pmatrix} 2F_m \\ 0 \\ 0 \end{pmatrix} \quad (24)$$

Here, ϕ_m , ϕ_{lg} , and ϕ_g denote the magnetic flux traversing: the permanent magnets, the total flux leakage from contiguous permanent magnets, back yoke and permanent magnets, and the air gap magnetic flux, respectively.

Through resolving the Eq. (24) and incorporating the differential equations, the various expressions for flux are formulated as mentioned:

$$\begin{cases} \phi_g = 0.5\phi_m - \frac{R_g+R_c+0.5R_{i2}}{R_g} \\ \phi_{lg} = \frac{R_g+R_c+0.5R_{i2}}{R_{lg}} \\ \phi_m = \frac{2F_m+R_g+R_c+0.5R_{i2}}{2R_m+2R_{i1}+0.5R_{lg}} \end{cases} \quad (25)$$

4 Determination of the torque

While induced currents are present in the conductor back yoke, their intensity is considerably lower in comparison to those generated in the conductor layer. Hence, during a rapid prediction and optimization process, it is permissible to neglect the EMF and torque originating from led disk back yoke. Moreover, it is crucial to recognize that the electromagnetic driving force predominantly acts on specific localized sub-divisions of the conductor thickness, via which the leading disk flux passes.

Presuming that V the volume taken by a permanent magnets single loop, the equivalent traction force can be expressed as mentioned:

$$W = \int_V |J \times B| dV = k_s J_m B_m t_c \tau_m (r_o - r_i) \quad (26)$$

where The Russell-Norsworthy coefficient k_s is utilized to evaluate the influence of the boundary effect induced by the 3-D eddy current:

$$k_s = 1 - \frac{\tanh[\pi L/2\tau_p]}{[\pi L/2\tau_p] \{1 + \tanh[L/2\tau_p] \tanh(\pi \Delta h/2\tau_p)\}} \quad (27)$$

With $L = (r_o - r_i)$.

Therefore, the electromagnetic torque generated by each loop is:

$$\Omega = r_m \left(\sum_{n=1}^{2N} W_n \right) \quad (28)$$

where W_n is the electromagnetic torque generated by loop 1 to loop 12 and $n = 1, 2, 3, \dots, 12$, symbolizes the quantity of loops and N is the quantity of copper grooves.

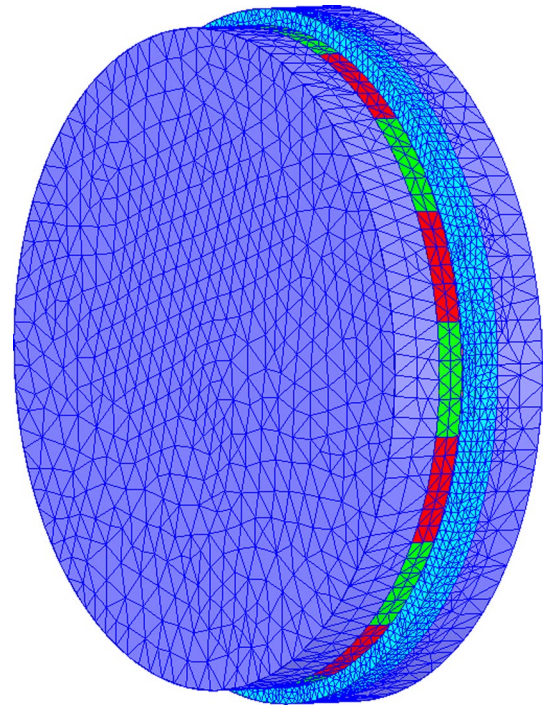
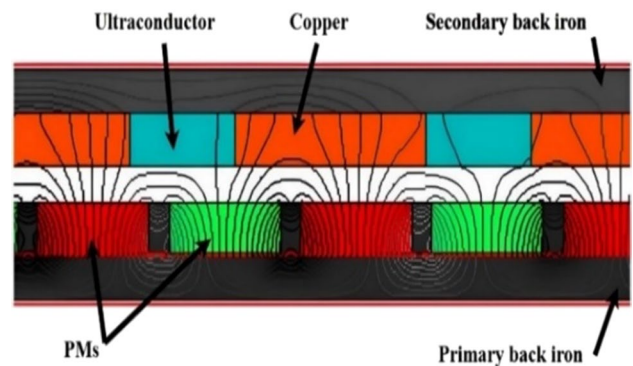
5 Findings and analysis

1) For motion body and boundary conditions setting

A geometrically regular polyhedron was created to enclose the moving parts, such as permanent magnets and the back iron, ensuring an adequate number of segments to maintain model integrity. The regular polyhedron was chosen as joint type, and relevant parameters were configured accordingly. Once the settings were finalised, a boundary was established to encompass all models, either manually or using the region command, taking into account the model's size for accurate representation.

2) Mesh division setting

The level of grid subdivision in simulating electromagnetic fields depends on the impact of material properties like permanent magnets, air gaps, copper conductor, ultra-conductor which required finer subdivision due to their influence

Fig. 6 NHUC's meshing model**Fig. 7** NHUC simulation's 2-D model

on the magnetic field. Materials with higher magnetic permeability, such as permanent magnet yoke iron and conductor yoke, have minimal impact, allowing for less stringent grid requirements. Balancing reasonable grid numbers with calculation convergence was crucial, with specific computer configuration demands for grid subdivision and solution. Figure 6 illustrates the grid meshing model of the hybrid ultra-conducting magnetic coupling.

3) Parameterization and solution settings

When dealing with simulation variables, solving them parametrically proves advantageous by eliminating repetitive model drawing, enhancing work efficiently. In the finite element model developed here, variables -speed difference (ns), air gap thickness (g), and magnetic field distribution (mf) are considered, with suitable solution intervals selected. Following this, a solution scheme is established, determining appropriate solution time and step size. With these pre-processing tasks completed, simulation analysis can commence after a thorough model check.

Figure 7 illustrates the simulation outcomes for NHUC's magnetic field density and flux of the. It is noticeable that the majority of the magnetic flux (depicted by solid lines) traverses the copper, while only a small portion crosses the ultra-conductor.

Iodine-doped carbon nanotubes is as the ultra-conductive material due to their superior performance compared to other types. The resistance of these nanotubes remains extremely low and relatively constant within the thermal span

Fig. 8 The relative resistance as a function of temperature [29]

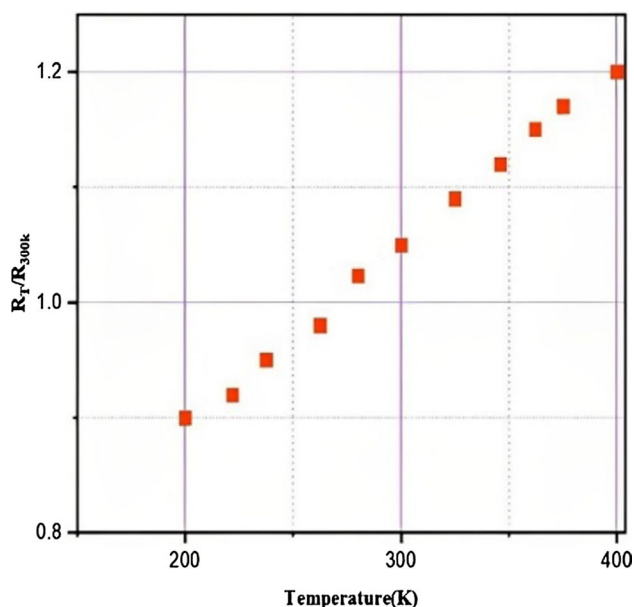
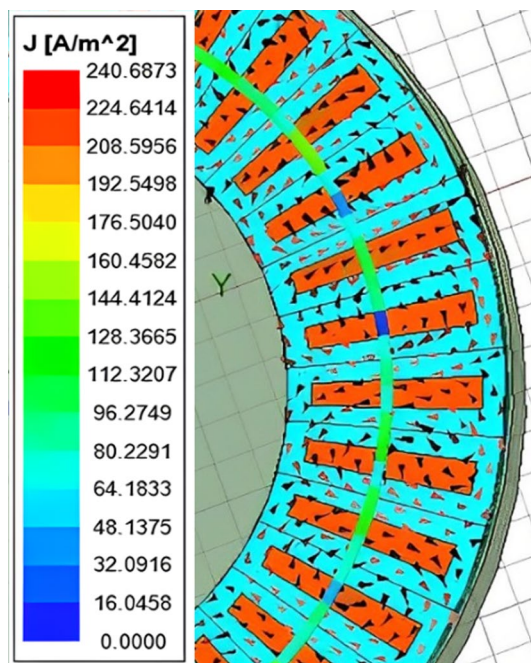


Fig. 9 The distribution of the eddy current on the magnetic coupling

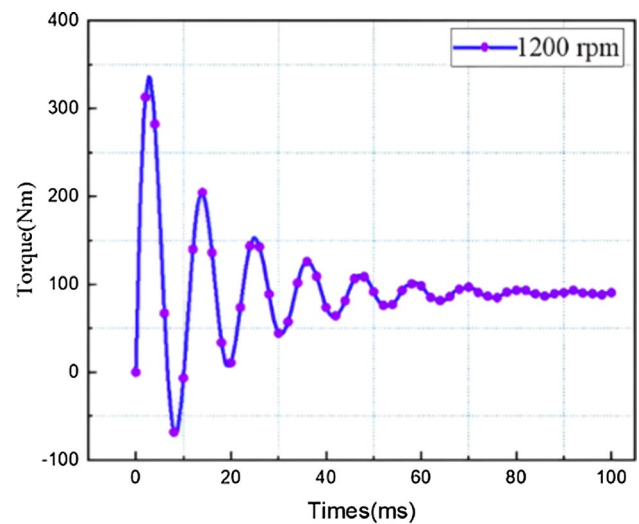


of 200 K to 400 K. The graph illustrating the relationship between its electrical resistance and temperature is presented in Fig. 8.

For a clearer insight into the focal points of heat concentration on the outside of the ultra-conductor disk, Fig. 9 displays the eddy current circulation while the coupling conveys optimal torque at a slip speed of 60 rpm. The illustration reveals that the eddy current forms ovaloid loops on different sections of the ultra-conductor disk. This phenomenon is attributed to the ultra-conductor’s extremely low reluctance, resulting in highest and dense eddy currents on the copper.

The torque performance of the NHUC at slip speeds of 1200 rpm is depicted in Fig. 10. The findings reveal that the NHUC is capable of transmitting a noteworthy maximum torque of 309 Nm at 1200 rpm, marking a substantial accomplishment in magnetic coupling. The incorporation of copper and the ultra-conductor, coupled with the ultra-conductor’s high conductivity, facilitates the creation of a dense magnetic field in the air gap, consequently enabling the transmission of high torque.

Fig.10 Torque opposing time, speed = 1200 rpm, g = 2 mm



Torque variation of overtime at various air gap distances is depicted in Fig. 11. The curves demonstrate that the torque values fluctuate with different air gap thicknesses. Specifically, at the lowest thickness, the torque can achieve a maximum magnitude of around 145 Nm. every curve exhibits a consistent pattern, characterized by an initial increase to a peak magnitude, followed by a decrease, and ultimately attaining a constant level.

Figure 12 illustrates an increase in the space between the leading disk and led disk components of the coupling results in a reduction in torque. Additionally, it is also observed that the curve illustrating the values obtained from the suggested MEC model closely aligns with the one depicting the 3D-FEM values, indicating the effectiveness of the model. The error is measured at 7.68% while the air gap thickness is 2 mm.

In Fig. 13, a gradual increase in the thickness of the PMs corresponds to an incremental rise in torque. A comparison between the results of the 3D simulation and those derived from the proposed MEC model is illustrated in both Figs. 12 and 13, revealing a close similarity between the two sets of outcomes. The consistent error observed between these values is attributed to the consideration, in the proposed MEC model, of the ultra-conductor's relatively low reluctance. Conversely, in the 3D-FEM, a permeability value close to zero is assigned to the ultra-conductor. The minor difference in values is a consequence of this slight disparity, visually evident relating the 3D-FEM and the suggested method.

Fig. 11 Torque opposing time at various air gap, hm = 10 mm, speed = 60 rpm

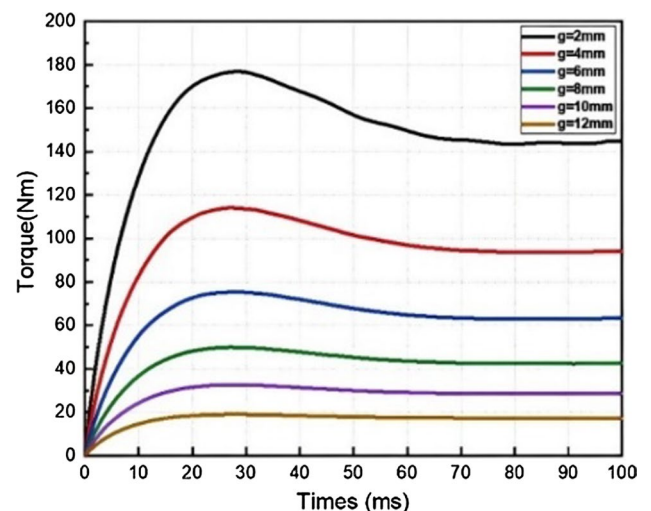


Fig. 12 Torque opposing air gap, speed = 60 rpm, time = 100 ms

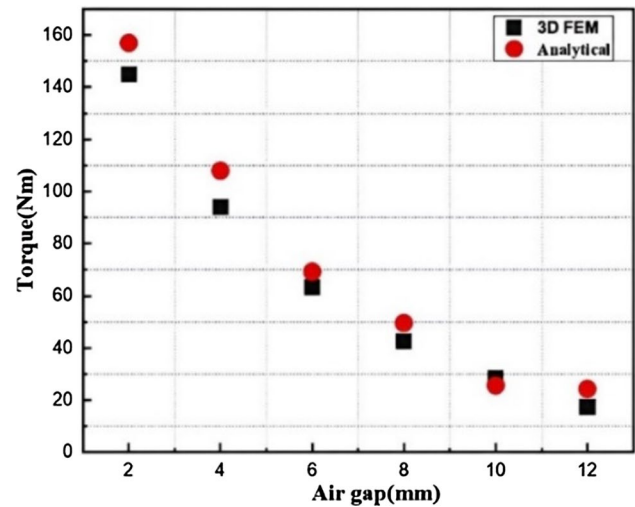
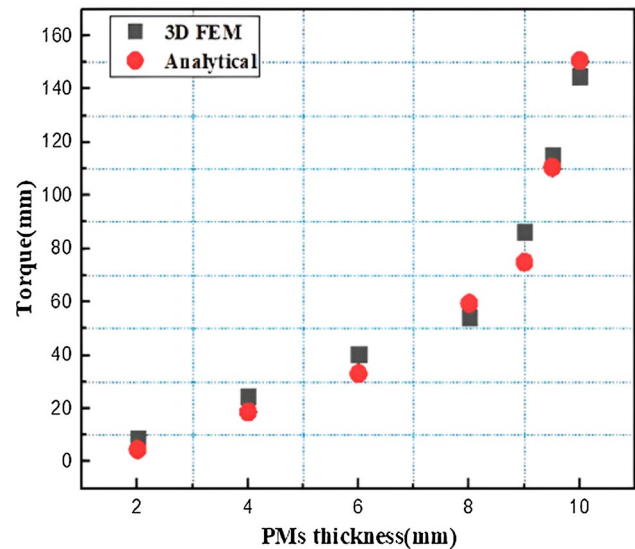


Fig. 13 Torque opposing PMs thickness, speed = 60 rpm, g = 2 mm, time = 100 ms



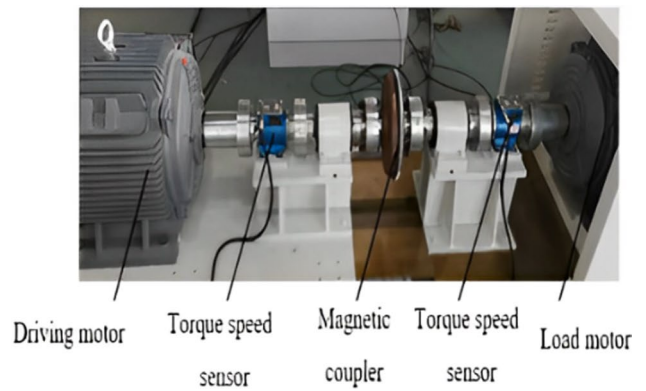
6 Comparison between the result obtained by the NHUC and the test result obtained by the slotted eddy current coupling (Sec)

A testing platform was established to assess the transmission and speed regulation capabilities of a magnetic coupling under various loads. Utilizing the motor-to-drag method, measurements were conducted, and the slotted eddy current magnetic coupling setup is illustrated in Fig. 14. It consists of the motor-to-drag test platform and a central computer with PID control to modify motor speed, startup mode, and signal feedback rate. Prior to testing, a crucial zero-reset operation is performed for optimal functionality.

A dedicated test platform, as shown in Fig. 14, was arranged for testing the magnetic coupling. Adjustments to the air gap thickness were made, and Table 2 presents test results for varying air gap thicknesses at a 60-rpm speed difference. The analysis compares outcomes of the slotted eddy current coupling with those from the NHUC.

In Fig. 15, the discrepancy between test results of the SEC and NHUC widens with increasing air gap. This variance is attributed to the NHUC's superior ability to maintain compactness compared to the SEC as the distance between components enlarges. The NHUC excels in efficient heat dissipation, safeguarding its conductivity against temperature elevation and preserving its compact nature. Unlike slotted eddy current couplings, the NHUC exhibits robust power transmission with minimal energy losses. Additionally, its proficiency in high-frequency operations makes it highly suitable for applications requiring potent and effective magnetic coupling.

Fig. 14 Test device of the Magnetic coupling, **a** motor platform test, **b** computer



(a)



(b)

Table 2 Comparative table of the test results of the SEC and the results of the FEM

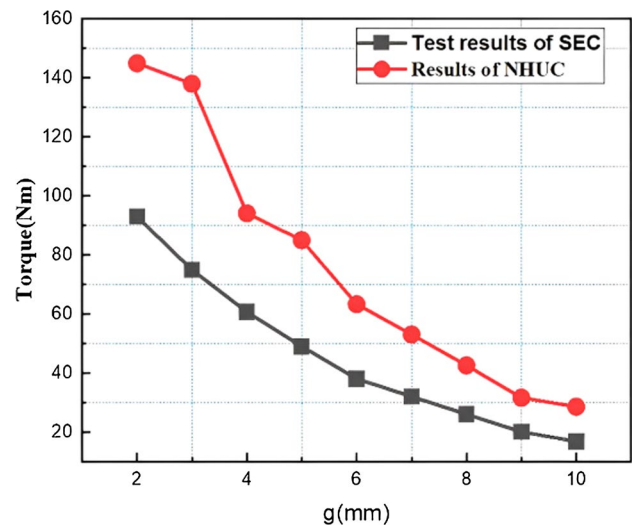
g (mm)	Electromagnetic Torque (Nm)	
	Test results SEC	Results of the NHUC
2	93	144.96
3	75	138.01
4	60.66	94.13
5	49	85
6	38	63.29
7	32	53.02
8	26	42.55
9	20	31.6
10	16.8	28.53

7 Conclusion

In this paper, we introduced a novel ultra-conductive coupling model, investigating its viability by alternating ultra-conductor and copper in the secondary under standard conditions. The research showed reduced losses due to the Joule effect with ultra-conductor surrounding copper. Findings for room temperature ultra-conductor include:

- The proposed model has been validated by observing the steadiness of the NHUC at both high and low speeds.

Fig. 15 Comparative torque of the test results of the SEC and the results of the FEM



- The data presented indicates a torque peak of 309 Nm at high speed and 145 Nm at low speed.
- An increase in air gap width results in a diminish in torque, while a grow in PMs thickness leads to an augment in electromagnetic torque.
- Induced currents are most pronounced on the ultra-conductor and least on the copper, forming loops.
- An error of 7.68% relating the findings calculated using the suggested model and those obtained from the simulation is exceptionally small, confirming the validity of the employed methodology.

Author contributions P.O.D conceived and designed the study, developed the novel hybrid ultra-conducting coupling (NHUC), and conducted the magnetic equivalent circuit (MEC) modeling. also investigated the impact of adjustments to air gap thickness and permanent magnet dimensions on torque variations.

Funding This project received partial funding from the National Natural Science Foundation of China under Grant 51875254, and partially from the Six Talent Peak Projects of Jiangsu Province under Grant 2015-ZBZZ-020.

Data availability The data supporting the findings of this study are available from the corresponding author upon reasonable request. The datasets generated and/or analysed during the current study are not publicly available but are accessible from the corresponding author upon reasonable request.

Declarations

Competing interests The authors affirm that they have no competing interests.

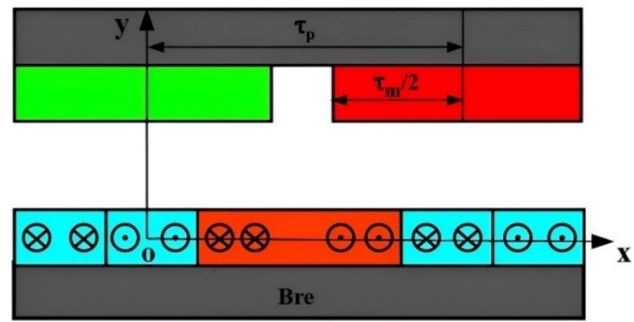
Open Access This article is licensed under a Creative Commons Attribution 4.0 International License, which permits use, sharing, adaptation, distribution and reproduction in any medium or format, as long as you give appropriate credit to the original author(s) and the source, provide a link to the Creative Commons licence, and indicate if changes were made. The images or other third party material in this article are included in the article's Creative Commons licence, unless indicated otherwise in a credit line to the material. If material is not included in the article's Creative Commons licence and your intended use is not permitted by statutory regulation or exceeds the permitted use, you will need to obtain permission directly from the copyright holder. To view a copy of this licence, visit <http://creativecommons.org/licenses/by/4.0/>.

Appendix

See Fig. 16

The eddy current density circulation in led disk impacts the deduction of the generated field formula for a specific loop. However, the deduction procedure remains identical. Takin in Fig. 2c loop as an instance, we determine the reaction field.

Fig. 16 Cartesian system defined for studying induced current reaction magnetic field



A cartesian system (Fig. 16) is determined, and, as per Ampere's loop theorem, the reaction fields at any position x within the middle zone $\tau_m/2 \leq x \leq \tau_p - \tau_m/2$ of the conductor can be depicted for right in dots and left in crosses, eddy currents.

In the midsection $\tau_m/2 \leq x \leq \tau_p - \tau_m/2$, the reaction magnetic field is formed by incoming (left) and outgoing (right) current bunches. Applying Ampere's theorem, the magnetic fields are derived for the current elements $J_m t_c dr$ of both incoming and outgoing currents at any point x .

$$2\pi(x-r)dB_R = \mu_0 J_m t_c dr \quad (29)$$

$$2\pi(r-x)dB_R = \mu_0 J_m t_c dr \quad (30)$$

consequently, the magnetic flux density on the position x is determined as mentioned:

$$B_R = \frac{\mu_0 J_m t_c}{2\pi} \left(\int_0^{\tau_m/2} \frac{dr}{x-r} + \int_{(\tau_p - \tau_m/2)}^{\tau_p} \frac{dr}{r-x} \right) = \frac{\mu_0 J_m t_c}{2\pi} \ln \frac{x\tau_p - x^2}{(x - \tau_m/2)(\tau_p - \tau_m/2 - x)} \quad (31)$$

Within $0 \leq x \leq \tau_m/2$, the reaction flux from the entry current cluster nullifies itself, leaving only the overall flux induced via outgoing current. The magnetic field from the reaction is expressed as follows:

$$B_R = \frac{\mu_0 J_m t_c}{2\pi} \int_{(\tau_p - \tau_m/2)}^{\tau_p} \frac{dr}{r-x} = \frac{\mu_0 J_m t_c}{2\pi} \ln \frac{\tau_p - x}{\tau_p - \tau_m/2 - x} \quad (32)$$

References

- Ye L, Member S, Li D, Ma Y, Jiao B. Design and performance of a water-cooled permanent magnet retarder for heavy vehicles. *IEEE Trans Energy Convers.* 2011;26:953–8.
- Dai X, et al. Analytical modeling of axial-flux permanent magnet eddy current couplings with a slotted conductor topology. *IEEE Trans Magn.* 2016;52:1–15.
- Li Z, Wang D, Zheng D. Accurate prediction and analysis of electromagnetic fields and forces in Flux-Focusing eddy current coupling with double slotted conductor rotors. *IEEE Access.* 2018;6:37685–99.
- Mohammadi S, Mirsalim M. Double-sided permanent-magnet radial-flux eddycurrent couplers: three-dimensional analytical modelling, static and transient study, and sensitivity analysis. *IET Electr Power Appl.* 2013;7:665–79.
- Yang X, Liu Y, Wang L. An improved analytical model of permanent magnet eddy current magnetic coupler based on electromagnetic-thermal coupling. *IEEE Access.* 2020;8:95235–50.
- Yang X, Liu Y, Wang L. Nonlinear modeling of transmission performance for permanent magnet eddy current coupler. *Math Probl Eng.* 2019;2019:1–14.
- Mohammadi S, Member S, Mirsalim M, Member S. Nonlinear modeling of eddy-current couplers. *IEEE Trans Energy Convers.* 2014;29:224–31.
- Mohammadi S, Member S, Mirsalim M, Member S, Vaez-zadeh S. Analytical modeling and analysis of axial-flux interior permanent-magnet couplers. *IEEE Trans Ind Electron.* 2014. <https://doi.org/10.1109/TIE.2014.2311391>.
- Aberoomand V, Mirsalim M, Fesharakifard R. Design optimization of double-sided permanent-magnet axial eddy-current couplers for use in dynamic applications. *IEEE Trans Energy Convers.* 2018. <https://doi.org/10.1109/TEC.2018.2880679>.
- Li Z, Zhang L, Qu B, Yang H, Wang D. Evaluation and analysis of novel flux-adjustable permanent magnet eddy current couplings with multiple rotors. *IET Electr Power Appl.* 2021;15:754–68.
- Xikang C, Wei L, Yang Z, Sitong L, Weiqi L. Method for pre-design of axial permanent magnetic coupler. *IEEE Trans Energy Convers.* 2019. <https://doi.org/10.1109/TEC.2019.2963713>.

12. Yang C, et al. Torque characteristics analysis of slotted-type eddy-current couplings using a new magnetic equivalent circuit model. *IEEE Trans Magn.* 2020;56:1–8.
13. Shi J, Suo S, Meng G. Theoretical calculation model of torque transmission in permanent-magnet couplers. *AIP Adv.* 2021;11: 025303.
14. Li Z, Wang D, Zheng D, Yu L. Analytical modeling and analysis of magnetic field and torque for novel axial flux eddy current couplers with PM excitation. *AIP Adv.* 2017;7: 105303.
15. Zheng D, et al. Eddy current loss calculation and thermal analysis of axial-flux permanent magnet couplers. *AIP Adv.* 2017;7: 025117.
16. Telezing BJK, et al. Torque characteristics analysis of a novel hybrid superconducting magnetic coupling with axial-flux using a magnetic equivalent circuit model. *IEEE Access.* 2022;10:45594–604.
17. Rallabandi V, Taran N, Ionel DM, Eastham JF. On the feasibility of carbon nanotube windings for electrical machines—case study for a coreless axial flux motor. 2016.
18. Raminosoa T, Aytug T. Impact of ultra-conducting winding on the power density and performance of non-heavy rare earth traction motors. In: 2019 IEEE Int Electr Mach Drives Conf IEMDC 2019. 2019. p. 2107–114. <https://doi.org/10.1109/IEMDC.2019.8785295>.
19. Yang C, Ombolo PD, Gao Y, Wang K, Yin X, Ruan S, KY, Boris J. Permanent magnet coupling with ultra-conductor and centrifugal speed regulator. CNPatentCN114337188B. p. 12. 2023.
20. Kumar RDS. Analysis of ultraconductors and superconductors. *Anveshana's Int J Res Eng Appl Sci.* 2019;4:24–32.
21. Li K, McGuire MA, Lupini AR, Skolrood L. Copper–carbon nanotube composites enabled by electrospinning for advanced conductors. *ACS Appl Nano Mater.* 2020. <https://doi.org/10.1021/acsnm.0c01236>.
22. Contreras E. Recent trends of nanomaterials for high-voltage applications. Amsterdam: Elsevier; 2018. p. 724–38. <https://doi.org/10.1016/B978-0-12-813351-4.00040-7>.
23. Janas D, Herman AP, Boncel S, Koziol KKK. Iodine monochloride as a powerful enhancer of electrical conductivity of carbon nanotube wires. *Carbon N.Y.* 2014;73:225.
24. Bucossi AR, et al. Enhanced electrical conductivity in extruded single-wall carbon nanotube wires from modified coagulation parameters and mechanical processing. *ACS Appl Mater Interfaces.* 2015;7:27299.
25. Bazbouz MB, Aziz A, Copic D, De Volder M, Welland ME. Fabrication of High specific electrical conductivity and high ampacity carbon nanotube/copper composite wires. *Adv Elect Materials.* 2021;7:2001213.
26. Cao M, et al. Ultrahigh electrical conductivity of graphene embedded in metals. *Adv Funct Mater.* 2019;1806792:1–8.
27. Magnesium FDAU, De Aquino F. Fran de Aquino. To cite this version : HAL Id : hal-03168776 Ultra-Conductive Magnesium. 2021.
28. Rallabandi V, Taran N, Ionel DM, Eastham JF. Coreless multidisc axial flux PM machine with carbon nanotube windings. *IEEE Trans Magn.* 2017;53:1–4.
29. Zhao Y, Wei J, Vajtai R, Ajayan PM, Barrera EV. Iodine doped carbon nanotube cables exceeding specific electrical conductivity of metals. *Sci Rep.* 2011;1:1–5.
30. Subramaniam C, et al. capacity in a carbon nanotube–copper composite. *Nat Commun.* 2013. <https://doi.org/10.1038/ncomms3202>.

Publisher's Note Springer Nature remains neutral with regard to jurisdictional claims in published maps and institutional affiliations.